



Evidence for Low-level Dynamical Excitation in Near-resonant Exoplanet Systems*

Malena Rice^{1,2}, Xian-Yu Wang³, Songhu Wang³, Avi Shporer², Khalid Barkaoui^{4,5,6}, Rafael Brahm^{7,8,9}, Karen A. Collins¹⁰, Andrés Jordán^{7,8,9}, Natalia Lowson¹¹, R. Paul Butler¹², Jeffrey D. Crane¹³, Stephen Shectman¹³, Johanna K. Teske¹², David Osip¹⁴, Kevin I. Collins¹⁵, Felipe Murgas^{16,17}, Gavin Boyle^{18,19}, Francisco J. Pozuelos^{4,20}, Mathilde Timmermans⁴, Emmanuel Jehin²¹, and Michaël Gillon⁴

¹Department of Astronomy, Yale University, New Haven, CT 06511, USA; malena.rice@yale.edu

²Department of Physics and Kavli Institute for Astrophysics and Space Research, Massachusetts Institute of Technology, Cambridge, MA 02139, USA

³Department of Astronomy, Indiana University, Bloomington, IN 47405, USA

⁴Astrobiology Research Unit, University of Liège, Allée du 6 août, 19, B-4000 Liège (Sart-Tilman), Belgium

⁵Department of Earth, Atmospheric and Planetary Sciences, MIT, 77 Massachusetts Avenue, Cambridge, MA 02139, USA

⁶Instituto de Astrofísica de Canarias (IAC), Calle Vía Láctea s/n, E-38200, La Laguna, Tenerife, Spain

⁷Millennium Institute for Astrophysics, Chile

⁸Facultad de Ingeniería y Ciencias, Universidad Adolfo Ibáñez, Av. Diagonal las Torres 2640, Peñalolén, Santiago, Chile

⁹Data Observatory Foundation, Chile

¹⁰Center for Astrophysics, Harvard & Smithsonian, 60 Garden Street, Cambridge, MA 02138, USA

¹¹Centre for Astrophysics, University of Southern Queensland, 499-565 West Street, Toowoomba, QLD 4350, Australia

¹²Carnegie Institution for Science, Earth & Planets Laboratory, 5241 Broad Branch Road NW, Washington, DC 20015, USA

¹³The Observatories of the Carnegie Institution for Science, 813 Santa Barbara Street, Pasadena, CA 91101, USA

¹⁴Las Campanas Observatory, Carnegie Institution for Science, Colina el Pino, Casilla 601 La Serena, Chile

¹⁵George Mason University, 4400 University Drive, Fairfax, VA, 22030 USA

¹⁶Instituto de Astrofísica de Canarias (IAC), E-38205 La Laguna, Tenerife, Spain

¹⁷Departamento de Astrofísica, Universidad de La Laguna (ULL), E-38206 La Laguna, Tenerife, Spain

¹⁸El Sauce Observatory—Obstech, Chile

¹⁹Cavendish Laboratory, JJ Thomson Avenue, Cambridge, CB3 0HE, UK

²⁰Instituto de Astrofísica de Andalucía (IAA-CSIC), Glorieta de la Astronomía s/n, E-18008 Granada, Spain

²¹Space Sciences, Technologies and Astrophysics Research (STAR) Institute, Université de Liège, Allée du 6 Août 19C, B-4000 Liège, Belgium

Received 2023 August 29; revised 2023 October 26; accepted 2023 November 1; published 2023 November 28

Abstract

The geometries of near-resonant planetary systems offer a relatively pristine window into the initial conditions of exoplanet systems. Given that near-resonant systems have likely experienced minimal dynamical disruptions, the spin–orbit orientations of these systems inform the typical outcomes of quiescent planet formation, as well as the primordial stellar obliquity distribution. However, few measurements have been made to constrain the spin–orbit orientations of near-resonant systems. We present a Rossiter–McLaughlin measurement of the near-resonant warm Jupiter TOI-2202 b, obtained using the Carnegie Planet Finder Spectrograph on the 6.5 m Magellan Clay Telescope. This is the eighth result from the Stellar Obliquities in Long-period Exoplanet Systems survey. We derive a sky-projected 2D spin–orbit angle $\lambda = 26^{+12}_{-15}^\circ$ and a 3D spin–orbit angle $\psi = 31^{+13}_{-11}^\circ$, finding that TOI-2202 b—the most massive near-resonant exoplanet with a 3D spin–orbit constraint to date—likely deviates from exact alignment with the host star’s equator. Incorporating the full census of spin–orbit measurements for near-resonant systems, we demonstrate that the current set of near-resonant systems with period ratios $P_2/P_1 \lesssim 4$ is generally consistent with a quiescent formation pathway, with some room for low-level ($\lesssim 20^\circ$) protoplanetary disk misalignments or post-disk-dispersal spin–orbit excitation. Our result constitutes the first population-wide analysis of spin–orbit geometries for near-resonant planetary systems.

Unified Astronomy Thesaurus concepts: Exoplanet astronomy (486); Exoplanet dynamics (490); Exoplanet migration (2205); Exoplanet formation (492); Exoplanet evolution (491); Orbital resonances (1181); Exoplanet systems (484); Exoplanets (498); Planetary alignment (1243); Orbital evolution (1178)

Supporting material: data behind figure

1. Introduction

The dynamical histories of planetary systems can, to some extent, be reconstructed through their current orbital demographics. Near-resonant systems, in which two or more planets exhibit near-exact integer ratio commensurabilities of their

orbital periods, offer an especially well-constrained lens into the evolution of planetary systems (e.g., Goldreich & Sciama 1965; Lee & Peale 2002; Millholland et al. 2018; Goyal et al. 2023). In these cases, formation models must jointly account for both the systems’ near-resonant configurations and their currently observed orbital geometries.

One observable constraint on a system’s orbital geometry is the tilt of companion planets’ orbits relative to the host star’s spin axis. The sky-projection of these “spin–orbit” angles, λ , can be measured for transiting planets through the Rossiter–McLaughlin effect (McLaughlin 1924; Rossiter 1924), in which small radial velocity (RV) shifts are observed across a transiting exoplanet’s passage in front of its host star. As the

* This paper includes data gathered with the 6.5 meter Magellan Telescopes located at Las Campanas Observatory, Chile.

planet transits, it sequentially blocks different red- and blueshifted components of the stellar disk, leading to a warped signal in the net observed Doppler shift across the transit. The profile of this warped signal encodes the degree of alignment between the planet’s transit path and the equator of the host star.

To date, only a handful of near-resonant systems have had spin–orbit angles measured to characterize the tilts of their constituent planetary orbits. In this work, we add a new measurement to this sample: a Rossiter–McLaughlin observation across a transit of the warm Jupiter TOI-2202 b. This is the eighth result from the Stellar Obliquities in Long-period Exoplanet Systems survey (Rice et al. 2021, 2022; Wang et al. 2022; Dong et al. 2023; Hixenbaugh et al. 2023; Rice et al. 2023; Wright et al. 2023), which examines the spin–orbit angles of relatively wide-orbiting transiting exoplanets.

TOI-2202 b lies in a near-resonant configuration deduced through observations of strong transit-timing variations (TTVs) from an expected outer companion near the 2:1 mean-motion resonance (MMR; Trifonov et al. 2021). Using newly obtained RV measurements from the Carnegie Planet Finder Spectrograph (PFS; Crane et al. 2006, 2008, 2010), together with archival data and new photometry from an assortment of telescopes, we derive a moderate 2D spin–orbit angle $\lambda = 26_{-15}^{+12}^\circ$ and 3D spin–orbit angle $\psi = 31_{-11}^{+13}^\circ$ for TOI-2202 b.

Combining our measurement with archival results, we conduct the first population study of the spin–orbit configurations of exoplanets with near-resonant companions. Our findings support the hypothesis that near-resonant planetary systems typically form quiescently—that is, within the disk plane and without violent post-disk-dispersal interactions, such as planet–planet scattering (Rasio & Ford 1996), which would significantly displace orbits from this initial plane—while simultaneously suggesting the prevalence of low-level dynamical excitation, even in near-resonant systems.

2. Observations

2.1. Photometric Monitoring

Because TOI-2202 b exhibits strong TTVs, we obtained several photometric transit observations leading up to the Rossiter–McLaughlin event to determine the optimal observing window. We also obtained simultaneous photometry during the scheduled Rossiter–McLaughlin observation to precisely constrain the transit midtime. Data from seven ground-based telescopes, described in the following subsections and shown in Figure 1, were used in this transit monitoring effort. Each transit of TOI-2202 b lasts 3.8 hr; however, most of our photometric monitoring included observations only at ingress to demonstrate the moving location of the transit start time. The derived transit midtimes associated with each set of observations are provided in Table 1 for reference.

2.1.1. MINERVA-Australis 0.7 m Photometry

Our team measured the ingress of TOI-2202 b’s transit on UT 2022 August 24 using one of the 0.7 m MINERVA-Australis telescopes (Addison et al. 2019) located at the University of Southern Queensland’s Mount Kent Observatory. The telescope is equipped with a 2000×2000 pixel Andor CCD with pixel scale $0''.608$, and we used a 15-pixel radius ($9''.12$) aperture to extract the photometry. We obtained 2.65 hr of

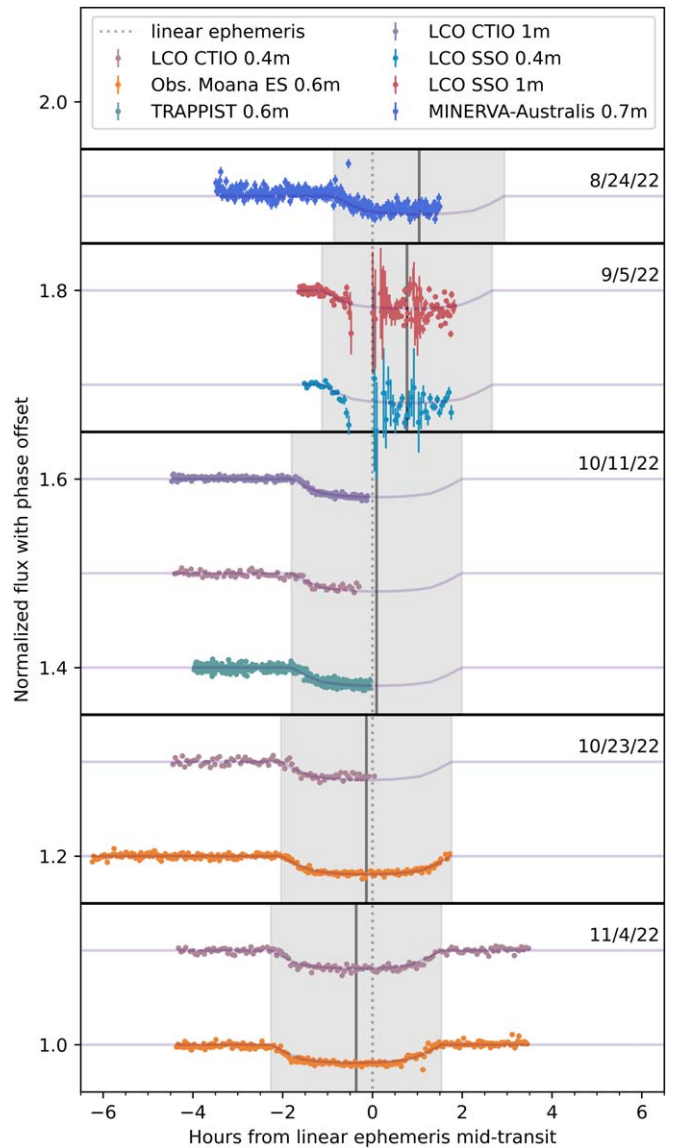


Figure 1. Photometry obtained from the seven telescopes used within this work. Observations are ordered by the date on which they were taken, with shaded regions signifying the modeled transit durations and solid gray lines denoting the transit midtimes measured for each dataset. The transit models associated with our parameter solution are shown together with the data, and a dotted line marks the linear ephemeris mid-transit. The dataset behind this figure is provided in the digital version of this manuscript.

(The data used to create this figure are available.)

pretransit baseline observations, as well as photometry during the first 2.25 hr of transit. Observations consisted of continuous 60 s broadband exposures. From this set of observations, we derived a 62.34 minutes late ingress of the transit relative to this work’s fitted linear ephemeris of TOI-2202 b.

2.1.2. LCOGT SSO 0.4 m and 1 m Photometry

We measured one partial transit of TOI-2202 b on UT 2022 September 9 using the Las Cumbres Observatory Global Network (LCOGT; Brown et al. 2013) Siding Spring Observatory (SSO) 0.4 and 1 m telescopes, in New South Wales in Australia. Observations were taken in the Sloan i' band with 170 s exposures on the 0.4 m telescope and 43 s

Table 1

Transit Numbers N , Midtransit Times t_0 , Uncertainties σ_{t_0} , and Offsets from the Linear Ephemeris Prediction Δ_{lin} for TOI-2202 b Based on our Collected Photometry and New TESS Transits Collected Since the Publication of Trifonov et al. (2021)

N	t_0 (BJD _{TDB})	σ_{t_0}	Δ_{lin} (min)	Instrument
–45	2459041.9141860	0.0013	44.91	TESS
–44	2459053.8287755	0.0012	46.98	TESS
–43	2459065.7370344	0.0010	39.93	TESS
–42	2459077.6478578	0.0010	36.58	TESS
–41	2459089.5520912	0.0014	23.74	TESS
–39	2459113.3622859	0.0016	0.54	TESS
–24	2459292.0300834	0.0013	–41.90	TESS
–23	2459303.9535926	0.0015	–26.98	TESS
–18	2459363.5678775	0.0017	42.90	TESS
–16	2459387.4048621	0.0016	58.28	TESS
20	2459816.2811297	0.0035	62.34	MINERVA-Australis
21	2459828.1830501	0.0029	46.16	LCOGT SSO 0.4 m LCOGT SSO 1 m
24	2459863.8942826	0.0020	5.52	LCOGT CTIO 0.4 m LCOGT CTIO 1 m
25	2459875.7978660	0.0014	–8.25	TRAPPIST-South LCOGT CTIO 0.4 m
26	2459887.7015528	0.0006	–21.88	Observatoire Moana ES LCOGT CTIO 1 m
36	2460006.8115743	0.0012	–52.83	Observatoire Moana ES TESS
37	2460018.7353190	0.0008	–37.58	TESS
38	2460030.6594249	0.0011	–21.80	TESS

Note. All listed Δ_{lin} values in this table are provided relative to our derived transit midtime epoch $T_0 = 2459577.9736362 \pm 0.0039$ days (Table 3).

exposures on the 1 m telescope. Photometry was extracted using the *AstroImageJ* software (Collins et al. 2017).

We obtained 0.38 and 0.51 hr of pretransit baseline observations, as well as photometry during the first 2.88 and 2.95 hr of transit, with the 0.4 and 1 m LCOGT SSO telescopes, respectively. Conditions were poor during this set of observations, impacting data obtained from both telescopes. Because transparency losses became significant only 30 minutes after the observed ingress, we were able to resolve a clear ingress that occurred 46.16 minutes late relative to this work’s fitted linear ephemeris of TOI-2202 b.

2.1.3. LCOGT CTIO 0.4 and 1 m Photometry

We also measured two transit ingress events for TOI-2202 b on UT 2022 October 10 and 2022 October 10, as well as one full transit on UT 2022 November 4, using the LCOGT Cerro Tololo Inter-American Observatory (CTIO) 0.4 m telescope located 80 km east of La Serena, Chile. The UT 2022 October 10 ingress was simultaneously observed using the LCOGT CTIO 1 m telescope. Observations were taken in the Sloan i' band, with 170 s exposures for the 0.4 m telescope observations and 43 s exposures for the 1 m telescope observations. Photometry was extracted using the *AstroImageJ* software (Collins et al. 2017).

From the 0.4 m LCOGT CTIO telescope, we obtained 2.60, 2.41, and 2.05 hr of pretransit photometry observations, as well as 1.50, 2.08, and 5.74 hr of postingress photometry observations during the evenings of UT 2022 October 11, 2022 October 23, and 2022 November 4, respectively. Our observations with the 1 m LCOGT CTIO telescope on UT

2022 October 11 included 2.66 hr of pretransit photometry observations, as well as 1.69 hr of in-transit data.

Based on the obtained LCOGT CTIO photometry, we found that the 2022 October 11 transit event of TOI-2202 b occurred 5.52 minutes late relative to this work’s fitted linear ephemeris of TOI-2202 b. The 2022 October 23 transit event occurred 8.25 minutes early, while the 2022 November 4 event occurred 21.88 minutes early.

2.1.4. TRAPPIST-South 0.6 m Photometry

We measured one transit egress event for TOI-2202 b on UT 2022 October 11 using the TRAPPIST-South 0.6 m robotic telescope (Gillon et al. 2011; Jehin et al. 2011) at La Silla Observatory in the Atacama Desert of Chile. Continuous 30 s observations were taken with the Astrodon “ $I+z$ ” filter. The TRAPPIST-South observing sequence spanned 2.16 hr prior to the transit ingress, as well as 1.76 in-transit hours of observations. The observed transit ingress time was consistent with the times derived from the simultaneous LCOGT CTIO 0.4 and 1 m observations taken on the same night (Section 2.1.3), with an ingress 5.52 minutes after the linear ephemeris prediction.

2.1.5. Observatoire Moana—El Sauce 0.6 m Photometry

Our team measured two full transits of TOI-2202 b on UT 2022 October 23 and UT 2022 November 4 using the station of the Observatoire Moana located in El Sauce Observatory (Ropert et al. 2021) in Chile. This station consists of a 0.6 m CDK robotic telescope coupled to an Andor iKon-L deep depletion 2000×2000 CCD with a scale of $0''.67$ per pixel. The second of these transits, on UT 2022 November 4, was obtained simultaneously with the presented Rossiter–McLaughlin measurement across the transit of TOI-2202 b. Observations were taken in the Sloan r band with continuous 100 s exposures.

The 2022 October 23 observations included nearly the full planet transit (3.76 in-transit hours), as well as 4.20 hr of pretransit baseline photometry. From this dataset, together with the LCOGT CTIO 1 m telescope observation described in Section 2.1.3, we derived an 8.25 minutes early ingress. The 2022 November 4 observation included 2.10 hr of pretransit and 1.91 hr of posttransit baseline observations, together with continuous observations throughout the transit itself.

2.2. Radial Velocity Observations

We observed the Rossiter–McLaughlin effect across one full transit of TOI-2202 b, from UT 00:48–8:35 on 2022 November 4, using the Carnegie Planet Finder Spectrograph (Crane et al. 2006, 2008, 2010) on the 6.5 m Magellan Clay telescope at Las Campanas Observatory in the southern Atacama Desert of Chile. Our team obtained 25 RV measurements, each with an exposure time of 1100 s, 3×3 binning, and typical RV precision ~ 3.1 m/s. Conditions were good throughout the observation, with typical seeing $0''.7$ – $0''.8$ and a small spike in seeing about an hour before transit. The airmass ranged from $z = 1.40$ to 1.77 through the observing sequence.

In addition to the transit itself, the observing sequence included 1.99 hr of pretransit and 1.72 hr of posttransit baseline observations. The PFS RV measurements obtained for this work are provided in Table 2 and shown in Figure 2.

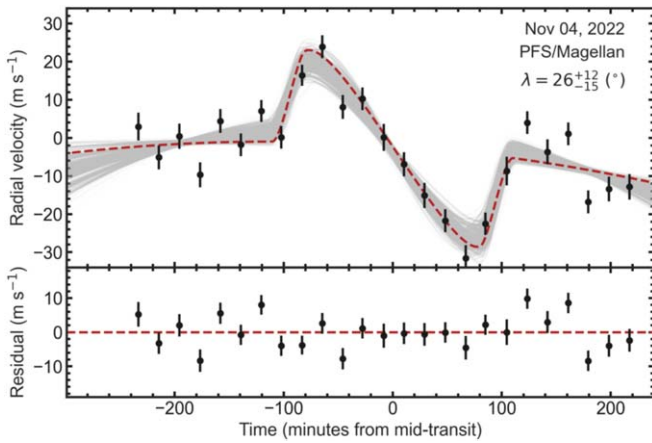


Figure 2. PFS observations of the TOI-2202 b Rossiter-McLaughlin effect from UT 11/4/22, together with the associated uncertainties and best-fitting model (red dashed line). Two thousand Rossiter-McLaughlin model draws from the posterior distribution are shown in gray. Residuals from the best-fitting model are provided in the lower panel.

Table 2

PFS RV Measurements for the TOI-2202 System, Obtained Across the Transit of TOI-2202 b

Time (BJD _{TDB})	RV (m s ⁻¹)	σ_{RV} (m s ⁻¹)
2459887.54038	2.96	3.65
2459887.55339	-5.13	3.14
2459887.56648	0.41	3.30
2459887.57971	-9.69	3.28
2459887.59266	4.42	3.13
2459887.60567	-1.81	2.98
2459887.61865	7.04	2.89
2459887.63136	0.10	2.94
2459887.64460	16.42	2.75
2459887.65761	23.90	3.05
2459887.67055	8.11	3.12
2459887.68319	10.25	3.00
2459887.69672	0.13	3.52
2459887.70952	-6.93	3.18
2459887.72273	-15.10	3.30
2459887.73584	-21.73	3.02
2459887.74891	-31.60	3.47
2459887.76152	-22.51	2.95
2459887.77497	-8.69	3.75
2459887.78803	3.99	2.96
2459887.80100	-3.67	3.26
2459887.81431	1.06	2.99
2459887.82690	-16.80	3.00
2459887.84022	-13.39	3.23
2459887.85314	-12.86	3.33

3. Global Fitting

3.1. Stellar Parameters

The EXOFASTv2 Python package (Eastman 2017; Eastman et al. 2019) was applied to derive precise stellar parameter values by fitting the host star’s spectral energy distribution (SED) using MESA Isochrones & Stellar Tracks (MIST; Choi et al. 2016; Dotter 2016) models. We constructed the SED using photometric measurements from 2MASS (Cutri et al. 2003), WISE (Cutri et al. 2021), and Gaia DR3 (Gaia Collaboration et al. 2023). Priors on stellar mass (M_*), age,

and effective temperature (T_{eff}) were adopted from Trifonov et al. (2021), while priors on parallax (ϖ) and upper limits on V-band extinction ($A(V)$) were drawn from Gaia DR3 and Schlafly & Finkbeiner (2011), respectively.

As noted by Eastman et al. (2023), incorporating transit-based densities can provide further constraints on stellar radius and mass, surpassing the limits of systematic error floors on stellar parameters (Tayar et al. 2022). Therefore, we included an additional likelihood term for stellar density in the stellar parameter fit to account for constraints imposed by the transit fit. The output stellar parameters are provided in the top section of Table 3. All derived stellar parameters are consistent with values reported in Trifonov et al. (2021) within 1σ .

3.2. Planetary System Parameters

We applied the `allesfitter` Python package (Günther & Daylan 2021) to refine the TOI-2202 planetary system parameters and derive the sky-projected spin-orbit angle of TOI-2202 b. Using `allesfitter`, we jointly modeled all photometry and RV observations obtained in this work, together with ten sectors of 30 minute cadence TESS (Ricker et al. 2015) photometry (Sectors 1, 2, 6, 9, 13, 27, 28, 29, 36, 39, 62, and 63)²² and all archival PFS, FEROS, and HARPS RVs, and ground-based transits reported in Trifonov et al. (2021).

The fitted parameters include the companion’s orbital period (P_b), the reference midtime epoch (T_0), all individual transit midtimes (t_0), the cosine of the planetary orbital inclination ($\cos i_b$), the planet-to-star radius ratio (R_b/R_*), the sum of radii divided by the orbital semimajor axis ($(R_* + R_b)/a_b$), the RV semi-amplitude (K_b), the parameterized orbital eccentricity and argument of periastron ($\sqrt{e_b} \cos \omega_b$, $\sqrt{e_b} \sin \omega_b$), the sky-projected spin-orbit angle (λ), the sky-projected stellar rotational velocity ($v \sin i_*$), and twelve limb-darkening coefficients, with two per photometric band (q_1 and q_2 for each of LCO, El Sauce, MINERVA, TRAPPIST-South, and TESS) and two for the in-transit RV dataset ($q_{1:RM}$ and $q_{2:RM}$). The systematic offsets between transit and RV data sets obtained by different instruments were accounted for by fitting and subtracting off a quadratic trend between each dataset. During the fit, the jitter term for each RV dataset was added in quadrature. We also fitted for the error scaling factor for each transit, normalized to the original photometric errors to ensure that only the relative weights are important. Parameters for planet c were held fixed at the values derived in Trifonov et al. (2021).

Posterior distributions were derived for each free parameter using an affine-invariant Markov chain Monte Carlo analysis, with 100 walkers that were each run to at least $30\times$ the autocorrelation length ($\geq 500,000$ accepted steps per walker) to ensure convergence. The resulting planetary parameters are provided in Table 3, while the transit midtimes t_0 derived for each light curve are listed in Table 1. The linear ephemeris was derived by applying a weighted least-squares fit to the set of output transit midtimes t_0 . The reference epoch was optimized to minimize the covariance between T_0 and P_b , and the resulting values are listed in Table 3. From this analysis, we derived a moderate sky-projected spin-orbit angle $\lambda = 26^{+12}_{-15}^\circ$ for TOI-2202 b, with the best-fitting model and residuals shown in Figure 2.

²² TESS data used in this paper can be found in MAST (STScI 2022).

Table 3
Priors and Posteriors for the TOI-2202 Planetary System

	Description (Units)	Priors	Fitted Value
Stellar parameters:			
M_*	Mass (M_\odot)	...	$0.841^{+0.034}_{-0.032}$
R_*	Radius (R_\odot)	...	$0.808^{+0.024}_{-0.022}$
T_{eff}	Effective temperature (K)	$\mathcal{N}(5144, 104)$	5169^{+80}_{-78}
$\log g$	Surface gravity (cgs)	$\mathcal{N}(4.55, 0.20)$	$4.548^{+0.030}_{-0.031}$
[Fe/H]	Metallicity (dex)	...	0.059 ± 0.043
$v \sin i_*$	Projected rotational velocity (km/s)	$\mathcal{U}(1.7; 0; 10)$	$2.14^{+0.28}_{-0.25}$
Age	Age (Gyr)	...	$6.4^{+4.4}_{-3.9}$
A_V	V-band extinction (mag)	$\mathcal{U}(0.242, 0.054)$	0.282 ± 0.047
ϖ	Parallax (mas)	$\mathcal{U}(4.226, 0.019)$	$4.225^{+0.016}_{-0.017}$
d	Distance (pc)	...	$236.69^{+0.95}_{-0.90}$
Planetary parameters:			
R_p/R_*	Planet-to-star radius ratio	$\mathcal{U}(0.125; 0; 1)$	$0.1265^{+0.0017}_{-0.0018}$
$(R_* + R_b)/a_b$	Sum of radii divided by orbital semimajor axis	$\mathcal{U}(0.043; 0; 1)$	$0.04336^{+0.00059}_{-0.00056}$
$\cos i_b$	Cosine of the orbital inclination	$\mathcal{U}(0.011; 0; 1)$	$0.0125^{+0.0020}_{-0.0029}$
P_b	Orbital period (days)	$\mathcal{U}(11.913; 10.913; 12.913)$	11.9126075 ± 0.00011
$T_{0,b}$	Midtime epoch (BJD _{TDB}) - 2458000 (days)	$\mathcal{U}(1578; 1577; 1579)$	1577.9736362 ± 0.0038
K_b	Radial velocity semi-amplitude (km/s)	$\mathcal{U}(0; 0; 10)$	$0.0907^{+0.0083}_{-0.0100}$
$\sqrt{e_b} \cos \omega_b$	Eccentricity parameter 1	$\mathcal{U}(0; -1; 1)$	$-0.059^{+0.089}_{-0.075}$
$\sqrt{e_b} \sin \omega_b$	Eccentricity parameter 2	$\mathcal{U}(0; -1; 1)$	$-0.04^{+0.14}_{-0.14}$
P_c	Orbital period (days)	fixed	24.7557
$T_{0,c}$	Midtime epoch (BJD _{TDB}) - 2458000 (days)	fixed	327.103
K_c	Radial velocity semi-amplitude (km/s)	fixed	0.0196
$\sqrt{e_c} \cos \omega_c$	Eccentricity parameter 1	fixed	-0.023
$\sqrt{e_c} \sin \omega_c$	Eccentricity parameter 2	fixed	-0.099
λ	Sky-projected spin-orbit angle ($^\circ$)	$\mathcal{U}(0; -180; 180)$	26^{+12}_{-15}
$q_{1,\text{LCO}}$	Linear limb-darkening coefficient for LCO	$\mathcal{U}(0.5; 0; 1)$	0.64 ± 0.24
$q_{2,\text{LCO}}$	Quadratic limb-darkening coefficient for LCO	$\mathcal{U}(0.5; 0; 1)$	$0.32^{+0.21}_{-0.13}$
$q_{1,\text{El Sauce}}$	Linear limb-darkening coefficient for El Sauce	$\mathcal{U}(0.5; 0; 1)$	$0.60^{+0.29}_{-0.36}$
$q_{2,\text{El Sauce}}$	Quadratic limb-darkening coefficient for El Sauce	$\mathcal{U}(0.5; 0; 1)$	$0.28^{+0.31}_{-0.20}$
$q_{1,\text{Minerva}}$	Linear limb-darkening coefficient for MINERVA	$\mathcal{U}(0.5; 0; 1)$	$0.43^{+0.24}_{-0.18}$
$q_{2,\text{MINERVA}}$	Quadratic limb-darkening coefficient for MINERVA	$\mathcal{U}(0.5; 0; 1)$	$0.37^{+0.32}_{-0.34}$
$q_{1,\text{TRAPPIST}}$	Linear limb-darkening coefficient for TRAPPIST	$\mathcal{U}(0.5; 0; 1)$	$0.43^{+0.19}_{-0.13}$
$q_{2,\text{TRAPPIST}}$	Quadratic limb-darkening coefficient for TRAPPIST	$\mathcal{U}(0.5; 0; 1)$	$0.56^{+0.23}_{-0.20}$
$q_{1,\text{TESS}}$	Linear limb-darkening coefficient for TESS	$\mathcal{U}(0.5; 0; 1)$	$0.32^{+0.20}_{-0.13}$
$q_{2,\text{TESS}}$	Quadratic limb-darkening coefficient for TESS	$\mathcal{U}(0.5; 0; 1)$	$0.45^{+0.27}_{-0.18}$
$q_{1,\text{PFS, RM}}$	Linear limb-darkening coefficient for the PFS RM	$\mathcal{U}(0.5; 0; 1)$	$0.72^{+0.20}_{-0.23}$
$q_{2,\text{PFS, RM}}$	Quadratic limb-darkening coefficient for the PFS RM	$\mathcal{U}(0.5; 0; 1)$	$0.56^{+0.28}_{-0.32}$
Derived parameters:			
M_b	Planetary mass (M_{Jup})	...	$0.904^{+0.087}_{-0.10}$
R_b	Planetary radius (R_{Jup})	...	0.977 ± 0.016
a_b/R_*	Semimajor axis over host radius	...	25.98 ± 0.34
i_b	Inclination ($^\circ$)	...	$89.29^{+0.17}_{-0.12}$
e_b	Eccentricity	...	$0.022^{+0.022}_{-0.015}$
ω_b	Argument of periastron ($^\circ$)	...	212^{+59}_{-94}
$T_{\text{tot},b}$	Total transit duration (days)	...	$3.768^{+0.032}_{-0.030}$
b	Impact parameter	...	$0.323^{+0.055}_{-0.080}$
$u_{1,\text{LCO}}$	Linear limb-darkening coefficient 1 for LCO	...	0.52 ± 0.19
$u_{2,\text{LCO}}$	Linear limb-darkening coefficient 2 for LCO	...	$0.28^{+0.27}_{-0.33}$
$u_{1,\text{El Sauce}}$	Linear limb-darkening coefficient 1 for El Sauce	...	$0.73^{+0.15}_{-0.18}$
$u_{2,\text{El Sauce}}$	Linear limb-darkening coefficient 2 for El Sauce	...	$-0.08^{+0.30}_{-0.24}$
$u_{1,\text{Minerva}}$	Linear limb-darkening coefficient 1 for MINERVA	...	$0.38^{+0.42}_{-0.27}$
$u_{2,\text{Minerva}}$	Linear limb-darkening coefficient 2 for MINERVA	...	$0.38^{+0.42}_{-0.27}$
$u_{1,\text{TRAPPIST}}$	Linear limb-darkening coefficient 1 for TRAPPIST	...	0.48 ± 0.30
$u_{2,\text{TRAPPIST}}$	Linear limb-darkening coefficient 2 for TRAPPIST	...	0.17 ± 0.37
$u_{1,\text{TESS}}$	Linear limb-darkening coefficient 1 for TESS	...	$0.51^{+0.13}_{-0.14}$
$u_{2,\text{TESS}}$	Linear limb-darkening coefficient 2 for TESS	...	$0.06^{+0.28}_{-0.25}$
$u_{1,\text{PFS, RM}}$	Linear limb-darkening coefficient 1 for the PFS RM	...	$0.88^{+0.46}_{-0.52}$
$u_{2,\text{PFS, RM}}$	Linear limb-darkening coefficient 2 for the PFS RM	...	$-0.09^{+0.52}_{-0.43}$

Note. P_b and T_0 were derived from the weighted least-square fit to the transit midtimes t_0 .

Trifonov et al. (2021) implemented a Gaussian process (GP) analysis to derive a stellar rotation period $P_{\text{rot}} = 24.1^{+2.3}_{-1.8}$ days for TOI-2202 based on TESS light curve data from Sectors 1,

2, 6, 9, and 13. To update this result, we reexamined the rotational period of TOI-2202 using the full set of currently available TESS data from Sectors 1, 2, 6, 9, 13, 27, 28, 29, 36,

39, 62, and 63, collected over a span of 1716 days from 2018 July 25 to 2023 April 6. We applied the GP kernels `SHOTerm` and `RotationTerm` that are encapsulated within the `celerite2` Python package (Foreman-Mackey 2018).

Four parallel chains were run using the `PyMC3` Python package (Salvatier et al. 2016) with an acceptance rate of 0.99, where each chain consisted of 10,000 tuning steps and 10,000 draws. Convergence was deemed to have been achieved when the Gelman–Rubin diagnostic (\hat{R} ; Gelman & Rubin 1992) fell below 1.01. The resulting stellar rotation period is $P_{\text{rot}} = 22 \pm 1$ days, corresponding to a stellar equatorial velocity $v = (2\pi R_*)/P_{\text{rot}} = 1.86 \pm 0.19 \text{ km s}^{-1}$.

Lastly, we combined v and $v \sin i_*$ to derive the stellar inclination i_* and the true stellar obliquity ψ for TOI-2202. The Bayesian inference method described in Masuda & Winn (2020) and Hjorth et al. (2021) was applied to account for the interdependent parameters v and $v \sin i_*$, and uniform priors were adopted for the three input parameters R_* , P_{rot} , and $\cos i$. This analysis yielded a stellar inclination estimate $i_* = 89^\circ.77 \pm 16^\circ.76$. Then, the true stellar obliquity (ψ) was derived through Equation (9) of Fabrycky & Winn (2009),

$$\cos \psi = \cos i_* \cos i + \sin i_* \sin i \cos \lambda, \quad (1)$$

where i_* is the stellar inclination and i is the planet’s orbital inclination. The resulting true stellar obliquity is $\psi = 31_{-11}^{+13}^\circ$.

4. Population Analysis of Near-resonant Systems

4.1. The Distribution of Spin–Orbit Angles for Near-resonant Exoplanets

To place this measurement into context, we examined the full set of transiting exoplanet systems with (1) a sky-projected spin–orbit measurement and (2) evidence that the transiting planet lies near a low-order mean-motion resonance with a neighboring companion. We initialized our sample by cross-matching the set of all exoplanets with λ measurements in the TEPcat catalog (Southworth 2011) with the set of exoplanets with one or more confirmed planetary companions around the same host star in the NASA Exoplanet Archive’s Planetary Systems table (NASA Exoplanet Archive 2023).²³ 32 planets were identified that fit these two criteria.²⁴

We also searched for any planets showing clear sinusoidal TTVs attributable to a resonant or near-resonant planetary companion that has not yet been directly confirmed. We identified all planets with (1) a spin–orbit measurement in the TEPcat catalog and (2) `ttv_flag=True` in the NASA Exoplanet Archive. In addition to TOI-2202 b, nine further candidate near-resonant planets were recovered in this manner. However, after closer examination, we concluded that, other than TOI-2202 b, none of the identified TTV planets without confirmed, nearby companions showed compelling sinusoidal signals (see Appendix for more details). Therefore, only TOI-2202 was added to the initial set of 32 identified systems with confirmed planetary companions.

Next, we identified systems within our sample with compact configurations near low-order resonances. The sample was restricted to include only systems for which the planet with a spin–orbit measurement has a small period ratio $P_2/P_1 \lesssim 4$ relative to at least one of its nearest neighbors. This limit was

selected for direct comparison with Figure 4 of Fabrycky et al. (2014). Both inner and outer planetary companions were considered, and the default parameter solution orbital periods from the NASA Exoplanet Archive were adopted for all planets. This cut left 19 planets in 16 systems, with properties described in Table 4.

The associated period ratio distribution is shown in Figure 3. The inner and outer period ratios for a single planet were included separately in cases where both met the criterion $P_2/P_1 \lesssim 4$. For systems in which more than one planet has a spin–orbit measurement (HD 3167, TRAPPIST-1, and V1298 Tau), each planet was separately considered and each relevant period ratio was included only once, for a total of 24 neighboring period ratios with $P_2/P_1 \lesssim 4$.

Lastly, we identified planets within the sample with at least one neighboring companion near a low-order orbital commensurability. Specifically, we searched for planet pairs that fall within 5% of the 2:1, 3:1, 4:1, 3:2, or 5:3 mean-motion commensurabilities. Most near-resonant pairs within the sample were found to lie just wide of the 2:1 and 3:2 resonances (see Figure 3), with a distribution comparable to that of the Kepler multitransiting systems examined in Fabrycky et al. (2014). In total, 13 near resonances were identified across twelve planet pairs.

The stellar obliquity distribution for these pairs as a function of host star T_{eff} is shown in Figure 4. As displayed in the top panel of Figure 4 and in Table 4, TOI-2202 b is the first exoplanet in a near-resonant configuration for which the measured sky-projected spin–orbit angle has not been consistent with exact alignment ($|\lambda| = 0^\circ$) within 1σ .

For six near-resonant systems, the 3D spin–orbit angle ψ has also been derived. These systems are shown in the bottom panel of Figure 4. The distribution of 3D angles reveals that a few more systems, in addition to TOI-2202 b, are likely offset from exact alignment. While no systems with near-resonant configurations have been found with strong misalignments indicative of polar or retrograde orbits, the scatter in the 3D distribution suggests some range in true stellar obliquities even in near-resonant systems.

To quantify this deviation from alignment, we drew 10,000 iterations of random values from each of the six systems with measured ψ values, using the reported Gaussian uncertainties from each measurement. Each iteration was then compared with an “aligned” Rayleigh distribution of 100,000 values, with scale parameter $\sigma = 1.8$ such that $\sim 98\%$ of draws fall within the range $\psi < 5^\circ$. A Kolmogorov–Smirnov test quantifying the difference between these two distributions returns $p < 0.05$ for 99.4% of random draws, whereas 0.6% of random draws return $p > 0.05$. As a result, we reject the null hypothesis that the observed ψ distribution exhibits consistent, near-exact ($\psi < 5^\circ$) alignment.

4.2. Additional Relevant Systems

A few systems were excluded from this population that may also serve to inform the distribution of spin–orbit angles for near-resonant systems. While these systems do not fit the criteria used to develop the uniform sample in Section 4.1, they each offer further relevant insights into the dynamical evolution of near-resonant exoplanet pairs.

One notable omission is a 1D spin–orbit measurement—obtained in the inclination direction—that indicates a misalignment in the compact multiplanet system Kepler-56

²³ Both catalogs were accessed on 7/20/2023.

²⁴ Because WASP-18 c is a contested planet, the WASP-18 system was removed from our sample.

Table 4
Systems with a Spin–Orbit Measurement and $P_2/P_1 \lesssim 4$

System	Planet	N_{pl}	Orbital Period (days)	MMR _{out}	MMR _{in}	$T_{\text{eff},*}$ (K)	$ \lambda $ ($^\circ$)	Reference, $ \lambda $	ψ ($^\circ$)
AU Mic	b	2	8.463000 ± 0.000002	3588 ± 87	$3.0_{-10.4}^{+10.3}$	Pallé et al. (2020)	$12.1_{-7.5}^{+11.3}$
HD 3167	c	4	29.8454 ± 0.0012	5261 ± 60	$108.9_{-5.4}^{+5.5}$	Bourrier et al. (2021)	$107.7_{-4.9}^{+5.1}$
HD 63433	b	2	$7.10793_{-0.00034}^{+0.00040}$	5640 ± 74	8_{-45}^{+33}	Mann et al. (2020)	$25.6_{-15.3}^{+22.5}$
HD 106315	c	2	21.05704 ± 0.00046	6327 ± 48	$2.7_{-2.7}^{+2.6}$	Bourrier et al. (2023)	...
Kepler-9 ^a	b	3	19.23891 ± 0.00006	...	2:1 (c:b)	5774 ± 60	13 ± 16	Wang et al. (2018)	$28.1_{-13.6}^{+13.0}$
Kepler-25 ^a	c	3	$12.72070_{-0.00010}^{+0.00011}$	2:1 (c:b)	...	6354 ± 27	0.5 ± 5.7	Albrecht et al. (2013)	$5.7_{-3.2}^{+4.2}$
Kepler-30 ^a	b	3	29.33434 ± 0.00815	...	2:1 (c:b)	5498 ± 54	1 ± 10	Sanchis-Ojeda et al. (2012)	...
Kepler-89	d	4	22.3429890 ± 0.0000067	2:1 (d:c)	...	6182 ± 58	6_{-13}^{+11}	Hirano et al. (2012)	...
TOI-942	b	2	4.324210 ± 0.000019	4969 ± 100	1_{-33}^{+41}	Wirth et al. (2021)	2_{-33}^{+27}
TOI-1136 ^a	d	6	$12.51937_{-0.00041}^{+0.00037}$	2:1 (d:c)	3:2 (e:d)	5770 ± 50	5 ± 5	Dai et al. (2023)	<28
TOI-2076 ^a	b	3	$10.35509_{-0.00014}^{+0.00020}$...	2:1 (c:b)	5187_{-53}^{+54}	3_{-15}^{+16}	Frazier et al. (2023)	18_{-11}^{+10}
TOI-2202 ^a	b	2	11.9126075 ± 0.00011	...	2:1 (c:b)	5169_{-80}^{+80}	26_{-12}^{+15}	this work	31_{-11}^{+13}
TRAPPIST-1 ^a	b	7	1.510826 ± 0.000006	...	4:1 (e:b)	2566 ± 26	15_{-30}^{+26}	Hirano et al. (2020)	$23.3_{-13.6}^{+17.0}$
TRAPPIST-1 ^a	e	7	6.101013 ± 0.000035	3:2 (e:d)	3:2 (f:e)	2566 ± 26	9_{-51}^{+45}	Hirano et al. (2020)	$23.3_{-13.6}^{+17.0}$
TRAPPIST-1 ^a	f	7	9.207540 ± 0.000032	3:2 (f:e)	2:1 (h:f)	2566 ± 26	21 ± 32	Hirano et al. (2020)	$23.3_{-13.6}^{+17.0}$
V1298 Tau ^a	b	4	24.1396 ± 0.0018	2:1 (b:d)	2:1 (e:b)	5050 ± 100	4_{-10}^{+7}	Johnson et al. (2022)	8_{-7}^{+4}
V1298 Tau ^a	c	4	8.24958 ± 0.00072	...	3:2 (d:c)	5050 ± 100	$4.9_{-15.1}^{+15.0}$	Feinstein et al. (2021)	...
WASP-47	b	4	4.1591492 ± 0.0000006	5552 ± 75	0 ± 24	Sanchis-Ojeda et al. (2015)	29_{-13}^{+11}
WASP-148 ^a	b	2	8.803809 ± 0.000043	...	4:1 (c:b)	5555 ± 90	$8.2_{-8.7}^{+9.7}$	Wang et al. (2022)	...

Notes. N_{pl} is the number of confirmed planets in the system to date. N_{pl} , orbital period, and $T_{\text{eff},*}$ have values drawn from the default parameter solution listed in the NASA Exoplanet Archive on 2023 July 7. Identified MMRs are provided for commensurabilities in which the listed planet is the outer (longer-period) planet of the pair, as well as those in which the listed planet is the inner (shorter-period) planet of the pair. References are provided for λ measurements. ψ values were drawn from Albrecht et al. (2021) when possible for systems with no measurement reported in TEPcat.

^a At least one low-order period commensurability has been identified in this system. The TRAPPIST-1 and TOI-1136 systems are each resonant chains, with additional commensurabilities within each system that are not listed in this table.

^b A single ψ value was derived for the TRAPPIST-1 system in Albrecht et al. (2021), such that these three values all correspond to just one measurement.

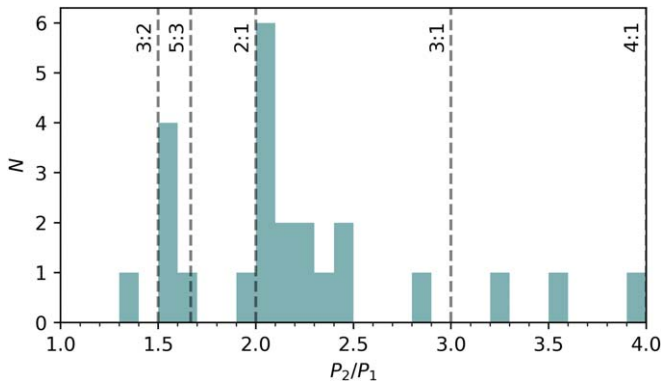


Figure 3. Period ratios of planet pairs in compact systems ($P_{\text{out}}/P_{\text{in}} \lesssim 4$) in which at least one planet has a spin–orbit measurement.

(Huber et al. 2013). This system was excluded because it does not have a reported λ constraint. Instead, an asteroseismic analysis conducted by Huber et al. (2013) revealed a stellar spin axis inclined at $i_* \sim 45^\circ$. The Kepler-56 system includes two transiting planets that, by definition, have $i_b \sim i_c \sim 90^\circ$, such that the stellar spin axis at $i_* \sim 45^\circ$ indicates a substantial misalignment in the line-of-sight direction. Kepler-56 b and c lie near a 2:1 (c:b) mean-motion commensurability.

Another relevant system is 55 Cancri, which is an aligned multiplanet system that includes a near-resonance (McArthur et al. 2004; Fischer et al. 2008; Nelson et al. 2014). This system was not included within our analysis because the only planet with a spin–orbit measurement in the system, 55 Cancri e, has a

large period ratio $P_b/P_e \sim 20$ with its nearest neighbor. However, a 3:1 near-resonance exists elsewhere in the system between 55 Cancri b and c, suggesting that this system may have formed in a similar manner to the systems in our sample. 55 Cancri e has a measured spin–orbit angle $\lambda = 10_{-20}^{+17^\circ}$ and $\psi = 23_{-12}^{+14^\circ}$ (Zhao et al. 2023).

A third relevant system is HIP 41378, with a previously reported misalignment $|\lambda| = 57_{-18}^{+26^\circ}$ for the planet HIP 41378 d (Grouffal et al. 2022). This system was excluded from the sample because the orbital period of HIP 41378 d has not been precisely confirmed. Only a partial Rossiter–McLaughlin observation has been obtained for this system due to the planet’s long transit duration, with measurement uncertainties in the acquired dataset that are comparable to the signal amplitude (Grouffal et al. 2022). HIP 41378 d provides an especially interesting case study as one of the few long-period transiting exoplanets that is amenable to spin–orbit measurements. Additional measurements would be helpful to more clearly establish whether this planet lies within a near-resonance and to more precisely constrain its spin–orbit configuration.

5. Discussion

The measured spin–orbit angle of TOI-2202 b, together with the full census of spin–orbit measurements for near-resonant exoplanets, indicates that even quiescently formed systems may experience low-level dynamical excitation that produces some dispersion in their spin–orbit orientations. The root of this excitation is intertwined with the underlying formation and prevalence of resonances in planetary systems.

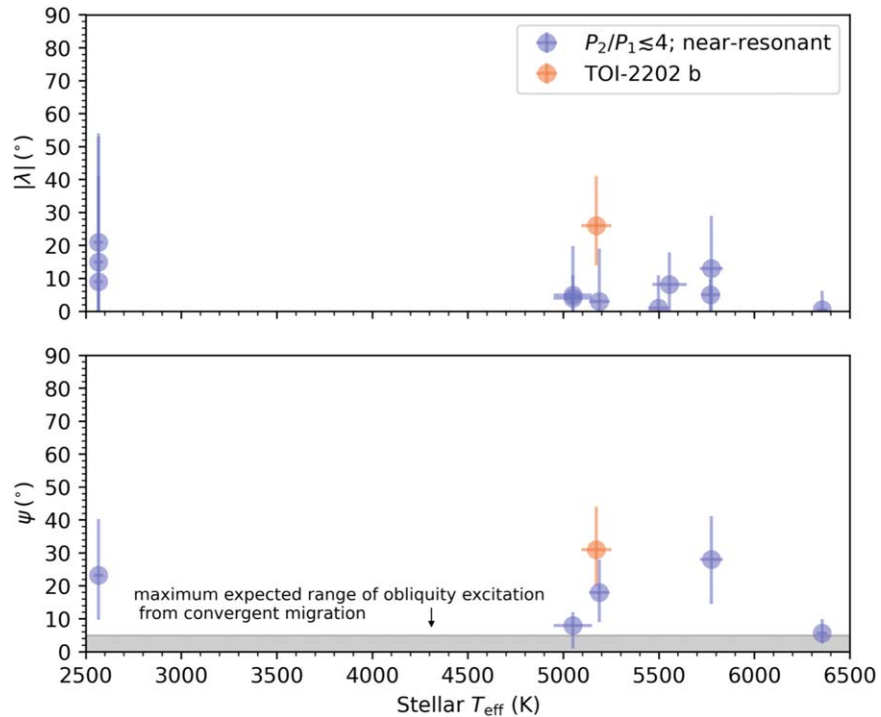


Figure 4. Sky-projected stellar obliquity $|\lambda|$ and 3D stellar obliquity ψ for near-resonant systems. The maximum expected level of stellar obliquity excitation in the convergent migration framework is shown in gray. All ψ values have been measured for separate planetary systems, while V1298 Tau and TRAPPIST-1 include two and three separate displayed $|\lambda|$ values, respectively.

At the population level, most near-resonant planets identified by Kepler have been observed to lie just wide of true mean-motion resonances (Lissauer et al. 2011; Fabrycky et al. 2014). This finding has been generally interpreted as evidence that such systems began in resonant configurations and were later displaced from deep resonance. Within this framework, near-resonant systems constitute a population that has successfully retained the imprints of past dynamical capture into mean-motion resonance—a delicate configuration that easily diverges from exact commensurability through post-disk-dispersal dynamical perturbations (e.g., Michtchenko et al. 2008a, 2008b; Deck et al. 2012; Izidoro et al. 2017; Leleu et al. 2021)—such that they offer key clues into their host systems’ primordial architectures.

Convergent migration (e.g., Goldreich & Sciama 1965; Snellgrove et al. 2001; Lee & Peale 2002; Rein 2012; Bitsch et al. 2019) could feasibly produce mean-motion resonances across a broad range of planetary systems. Planet pairs may be gently pushed away from nominal mean-motion resonances in the post-disk-dispersal stage through eccentricity damping and orbital circularization (Terquem & Papaloizou 2007; Lithwick & Wu 2012; Batygin & Morbidelli 2013; Delisle et al. 2014; Goldreich & Schlichting 2014; Chatterjee & Ford 2015) or through in situ mass growth by planets on circular orbits (Petrovich et al. 2013).

Convergent migration and gentle resonance divergence mechanisms are expected to operate within the plane of the host protoplanetary disk. Even in the more dynamically violent instability framework modeled by Izidoro et al. (2017), the spin-orbit distribution of planets formed within aligned protoplanetary disks is expected to peak at $\psi \leq 5^{\circ}$ (Esteves et al. 2023) from the process of resonance disruption alone. Therefore, nonzero spin-orbit misalignments may trace small primordial tilts of the systems’ natal protoplanetary disks.

Previous studies examining the mutual inclinations between stellar rotation axes and their surrounding protoplanetary (Davies 2019) and debris (Hurt & MacGregor 2023) disks have each demonstrated evidence consistent with a prevalence of low-level ($\lesssim 20^{\circ}$) disk misalignments that could be attributed solely to chaotic accretion in turbulent molecular cloud cores (Takaishi et al. 2020).

Alternatively, low-level misalignments in near-resonant systems may be produced by a mechanism that does not require a primordially misaligned inner disk. For example, Gratia & Fabrycky (2017) showed that planet-planet scattering in the outer region of a planetary system may gently produce small misalignments of up to $\sim 20^{\circ}$ in the inner planetary system, offering a possible avenue to tilt a system without disrupting near resonances. A misaligned outer planet, produced through either planet-planet scattering in the outer system or through a misaligned outer disk (e.g., Nealon et al. 2019), could also potentially tilt its inner companions (Zhang et al. 2021) while preserving a near-resonant configuration.

The planets in compact, near-resonant systems considered within this work span a range of masses, from sub-Earth-mass (TRAPPIST-1 e at $0.692 \pm 0.022 M_{\oplus}$; Agol et al. 2021) to Jovian-mass planets (TOI-2202 b at $0.904^{+0.087}_{-0.10} M_J$; this work). This wide range of planet masses may encompass multiple regimes of planet formation and migration that have not been disentangled within our analysis. The current set of observations does not demonstrate a clear distinction between the spin-orbit angles of lower- and higher-mass planets in near-resonant configurations. An expanded sample may unveil population differences, if present, across mass regimes.

Further monitoring of the TOI-2202 system is needed to more precisely pinpoint the properties of the TOI-2202c planet and to constrain the presence of additional companions within the system. A direct confirmation of TOI-2202c would offer the

opportunity to demonstrate whether the system lies within, or only near, a “true” resonance, such that a critical angle in the system librates about a fixed point. More broadly, additional high-precision Rossiter–McLaughlin measurements for near-resonant systems offer a promising path forward to constrain the origins of low-level misalignments in quiescently formed systems.

Across the broader population of exoplanets with spin–orbit measurements—including those that are not in near-resonant systems—previous work has found evidence for a nonzero mean stellar obliquity with significant scatter $\psi = 19^\circ \pm 10^\circ$ (Muñoz & Perets 2018). The apparent persistence of this deviation from alignment, even in near-resonant systems, suggests the universality of low-level dynamical excitation—a pattern well exemplified by the TOI-2202 system.

Acknowledgments

We thank the anonymous referee for their valuable feedback on this manuscript. We thank Chelsea Huang for the support in organizing observations for this work. M.R. and S.W. thank the Heising-Simons Foundation for their generous support. M.R. acknowledges support from Heising-Simons Foundation Grant #2023-4478, as well as the 51 Pegasi b Fellowship Program. This paper includes data gathered with the 6.5 m Magellan Telescopes located at Las Campanas Observatory, Chile. This research has made use of the NASA Exoplanet Archive, which is operated by the California Institute of Technology, under contract with the National Aeronautics and Space Administration under the Exoplanet Exploration Program. A.J. acknowledges support from ANID—Millennium Science Initiative—ICN12_009 and FONDECYT project 1210718. R.B. acknowledges support from FONDECYT project 11200751 and additional support from ANID—Millennium Science Initiative—ICN12_009.

This work makes use of observations from the LCOGT network. Part of the LCOGT telescope time was granted by NOIRLab through the Mid-Scale Innovations Program (MSIP). MSIP is funded by NSF. This research has made use of the Exoplanet Follow-up Observation Program (ExoFOP; DOI: 10.26134/ExoFOP5) website, which is operated by the California Institute of Technology, under contract with the National Aeronautics and Space Administration under the Exoplanet Exploration Program. K.A.C. acknowledges support from the TESS mission via subaward s3449 from MIT.

This work makes use of data from the MINERVA-Australis facility. MINERVA-Australis is supported by Australian Research Council LIEF Grant LE160100001, Discovery Grants DP180100972 and DP220100365, Mount Cuba Astronomical Foundation, and institutional partners University of Southern Queensland, UNSW Sydney, MIT, Nanjing University, George Mason University, University of Louisville, University of California Riverside, University of Florida, and The University of Texas at Austin. We respectfully acknowledge the traditional custodians of all lands throughout Australia, and recognize their continued cultural and spiritual connection to the land, waterways, cosmos, and community. We pay our deepest respects to all Elders, ancestors and descendants of the Giabal, Jarowair, and Kambuwal nations, upon whose lands the MINERVA-Australis facility at Mt Kent is situated.

TRAPPIST-South is funded by the Belgian National Fund for Scientific Research (F.R.S.-FNRS) under grant PDR T.0120.21, with the participation of the Swiss National Science

Foundation (SNF). M.G. and E.J. are FNRS Senior Research Associates. The postdoctoral fellowship of K.B. is funded by F.R.S.-FNRS grant T.0109.20 and by the Francqui Foundation. F.J.P. acknowledges financial support from the grant CEX2021-001131-S funded by MCIN/AEI/ 10.13039/501100011033. This publication benefits from the support of the French Community of Belgium in the context of the FRIA Doctoral Grant awarded to MT. This research was supported in part by Lilly Endowment, Inc., through its support for the Indiana University Pervasive Technology Institute.

Facility: Magellan:Clay (PFS); MINERVA-Australis; LCOGT (SSO 0.4 m and 1m); LCOGT (CTIO 0.4 m and 1m); TRAPPIST (South 0.6m); El Sauce: 0.6m; NASA Exoplanet Archive.

Software: allesfitter (Günther & Daylan 2021), AstroImageJ (Collins et al. 2017), emcee (Foreman-Mackey et al. 2013), lightkurve (Lightkurve Collaboration et al. 2018), matplotlib (Hunter 2007), numpy (Oliphant 2006; Walt et al. 2011; Harris et al. 2020), pandas (McKinney 2010), ptemcee (Vousden et al. 2016), scipy (Virtanen et al. 2020).


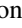

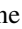







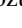

Appendix Vetting TTV Planets

Here, we discuss the vetting process applied in Section 4 to identify planets with observed TTVs that are likely indicative of near-resonant companions. The candidate planets with spin–orbit measurements and with TTV signals, but with no confirmed planet attributable to the TTV signal, include CoRoT-2 b, HAT-P-13 b, KELT-19 A b, KOI-12 b, KOI-13 b, Kepler-17 b, Qatar-1 b, WASP-12 b, and WASP-43 b.

None of the identified TTV planets without confirmed, nearby companions included clear sinusoidal signals. WASP-12 b and Qatar-1 b were removed from the sample, since both systems have been monitored and found to show no sinusoidal TTVs (Collins et al. 2017). We note that the Qatar-1 b TTV detection has also been contested (von Essen et al. 2013; Maciejewski et al. 2015). Likewise, WASP-12 b demonstrates transit-timing variations that previous studies have found are most consistent with a decaying orbit (Yee et al. 2020; Turner et al. 2021; Wong et al. 2022). The TTV observations of WASP-43 b have also been attributed to orbital decay (Jiang et al. 2016), which was later ruled out (Hoyer et al. 2016; Garai et al. 2021); however, the WASP-43 b TTVs show no clear signs of periodicity. No clear periodicities were identified in the CoRoT-2 b, HAT-P-13 b, or KELT-19 A b TTVs based on the results reported in Ivshina & Winn (2022). Holczer et al. (2016) found that the frequency of Kepler-17 b’s TTVs may be attributable to the star’s rotational frequency, and that the TTVs of KOI-13 b show a strong stroboscopic effect such that they may not be associated with a companion planet. Holczer et al. (2016) also identified no clearly sinusoidal periodicity in the TTVs observed for KOI-12 b.

ORCID iDs

Malena Rice  <https://orcid.org/0000-0002-7670-670X>
 Xian-Yu Wang  <https://orcid.org/0000-0002-0376-6365>
 Songhu Wang  <https://orcid.org/0000-0002-7846-6981>
 Avi Shporer  <https://orcid.org/0000-0002-1836-3120>
 Khalid Barkaoui  <https://orcid.org/0000-0003-1464-9276>
 Rafael Brahm  <https://orcid.org/0000-0002-9158-7315>
 Karen A. Collins  <https://orcid.org/0000-0001-6588-9574>

Andrés Jordán  <https://orcid.org/0000-0002-5389-3944>
 Natalia Lowson  <https://orcid.org/0000-0001-6508-5736>
 R. Paul Butler  <https://orcid.org/0000-0003-1305-3761>
 Jeffrey D. Crane  <https://orcid.org/0000-0002-5226-787X>
 Stephen Shectman  <https://orcid.org/0000-0002-8681-6136>
 Johanna K. Teske  <https://orcid.org/0009-0008-2801-5040>
 David Osip  <https://orcid.org/0000-0003-0412-9664>
 Kevin I. Collins  <https://orcid.org/0000-0003-2781-3207>
 Felipe Murgas  <https://orcid.org/0000-0001-9087-1245>
 Gavin Boyle  <https://orcid.org/0009-0009-2966-7507>
 Francisco J. Pozuelos  <https://orcid.org/0000-0003-1572-7707>
 Emmanuel Jehin  <https://orcid.org/0000-0001-8923-488X>
 Michaël Gillon  <https://orcid.org/0000-0003-1462-7739>

References

- Addison, B., Wright, D. J., Wittenmyer, R. A., et al. 2019, *PASP*, **131**, 115003
 Agol, E., Dorn, C., Grimm, S. L., et al. 2021, *PSJ*, **2**, 1
 Albrecht, S., Winn, J. N., Marcy, G. W., et al. 2013, *ApJ*, **771**, 11
 Albrecht, S. H., Marcussen, M. L., Winn, J. N., Dawson, R. I., & Knudstrup, E. 2021, *ApJL*, **916**, L1
 Batygin, K., & Morbidelli, A. 2013, *AJ*, **145**, 1
 Bitsch, B., Izidoro, A., Johansen, A., et al. 2019, *A&A*, **623**, A88
 Bourrier, V., Attia, O., Mallonn, M., et al. 2023, *A&A*, **669**, A63
 Bourrier, V., Lovis, C., Cretignier, M., et al. 2021, *A&A*, **654**, A152
 Brown, T., Baliber, N., Bianco, F., et al. 2013, *PASP*, **125**, 1031
 Chatterjee, S., & Ford, E. B. 2015, *ApJ*, **803**, 33
 Choi, J., Dotter, A., Conroy, C., et al. 2016, *ApJ*, **823**, 102
 Collins, K. A., Kielkopf, J. F., & Stassun, K. G. 2017, *AJ*, **153**, 78
 Collins, K. A., Kielkopf, J. F., Stassun, K. G., & Hessman, F. V. 2017, *AJ*, **153**, 77
 Crane, J. D., Shectman, S. A., & Butler, R. P. 2006, *Proc. SPIE*, **6269**, 972
 Crane, J. D., Shectman, S. A., Butler, R. P., et al. 2010, *Proc. SPIE*, **7735**, 1909
 Crane, J. D., Shectman, S. A., Butler, R. P., Thompson, I. B., & Burley, G. S. 2008, *Proc. SPIE*, **7014**, 2484
 Cutri, R. M., Skrutskie, M. F., van Dyk, S., et al. 2003, *Vizie Online Data Catalog*, II/246
 Cutri, R. M., et al. 2021, *Vizie Online Data Catalog*, II/328
 Dai, F., Masuda, K., Beard, C., et al. 2023, *AJ*, **165**, 33
 Davies, C. L. 2019, *MNRAS*, **484**, 1926
 Deck, K. M., Holman, M. J., Agol, E., et al. 2012, *ApJL*, **755**, L21
 Delisle, J.-B., Laskar, J., & Correia, A. 2014, *A&A*, **566**, A137
 Dong, J., Wang, S., Rice, M., et al. 2023, *ApJL*, **951**, L29
 Dotter, A. 2016, *ApJS*, **222**, 8
 Eastman, J., 2017 EXOFASTv2: Generalized Publication-quality Exoplanet Modeling Code, Astrophysics Source Code Library, ascl:1710.003
 Eastman, J. D., Diamond-Lowe, H., & Tayar, J. 2023, *AJ*, **166**, 132
 Eastman, J. D., Rodriguez, J. E., Agol, E., et al. 2019, arXiv:1907.09480
 Esteves, L., Izidoro, A., Winter, O. C., Bitsch, B., & Isella, A. 2023, *MNRAS*, **521**, 5776
 Fabrycky, D. C., Lissauer, J. J., Ragozzine, D., et al. 2014, *ApJ*, **790**, 146
 Fabrycky, D. C., & Winn, J. N. 2009, *ApJ*, **696**, 1230
 Feinstein, A. D., Montet, B. T., Johnson, M. C., et al. 2021, *AJ*, **162**, 213
 Fischer, D. A., Marcy, G. W., Butler, R. P., et al. 2008, *ApJ*, **675**, 790
 Foreman-Mackey, D. 2018, *RNAAS*, **2**, 31
 Foreman-Mackey, D., Hogg, D. W., Lang, D., & Goodman, J. 2013, *PASP*, **125**, 306
 Frazier, R. C., Stefánsson, G., Mahadevan, S., et al. 2023, *ApJL*, **944**, L41
 Gaia Collaboration, Vallenari, A., & Brown, A. G. A. 2023, *A&A*, **674**, A1
 Garai, Z., Pribulla, T., Parviainen, H., et al. 2021, *MNRAS*, **508**, 5514
 Gelman, A., & Rubin, D. B. 1992, *StaSc*, **7**, 457
 Gillon, M., Jehin, E., Magain, P., et al. 2011, *EPJ Web of Conferences*, **11**, 06002
 Goldreich, P., & Schlichting, H. E. 2014, *AJ*, **147**, 32
 Goldreich, P., & Sciama, D. 1965, *MNRAS*, **130**, 159
 Goyal, A. V., Dai, F., & Wang, S. 2023, *ApJ*, **955**, 118
 Gratia, P., & Fabrycky, D. 2017, *MNRAS*, **464**, 1709
 Grouffal, S., Santerne, A., Bourrier, V., et al. 2022, *A&A*, **668**, A172
 Günther, M. N., & Daylan, T. 2021, *ApJS*, **254**, 13
 Harris, C. R., Millman, K. J., van der Walt, S. J., et al. 2020, *Natur*, **585**, 357
 Hirano, T., Gaidos, E., Winn, J. N., et al. 2020, *ApJL*, **890**, L27
 Hirano, T., Narita, N., Sato, B., et al. 2012, *ApJL*, **759**, L36
 Hixenbaugh, K., Wang, X.-Y., Rice, M., & Wang, S. 2023, *ApJL*, **949**, L35
 Hjorth, M., Albrecht, S., Hirano, T., et al. 2021, *PNAS*, **118**, e2017418118
 Holczer, T., Mazeh, T., Nachmani, G., et al. 2016, *ApJS*, **225**, 9
 Hoyer, S., Pallé, E., Dragomir, D., & Murgas, F. 2016, *AJ*, **151**, 137
 Huber, D., Carter, J. A., Barbieri, M., et al. 2013, *Sci*, **342**, 331
 Hunter, J. D. 2007, *CSE*, **9**, 90
 Hurt, S. A., & MacGregor, M. A. 2023, *ApJ*, **954**, 10
 Ivshina, E. S., & Winn, J. N. 2022, *ApJS*, **259**, 62
 Izidoro, A., Ogihara, M., Raymond, S. N., et al. 2017, *MNRAS*, **470**, 1750
 Jehin, E., Gillon, M., Queloz, D., et al. 2011, *Msngr*, **145**, 2
 Jiang, I.-G., Lai, C.-Y., Savushkin, A., et al. 2016, *AJ*, **151**, 17
 Johnson, M. C., David, T. J., Pettigura, E. A., et al. 2022, *AJ*, **163**, 247
 Lee, M. H., & Peale, S. J. 2002, *ApJ*, **567**, 596
 Leleu, A., Alibert, Y., Hara, N., et al. 2021, *A&A*, **649**, A26
 Lightkurve Collaboration, Cardoso, J. V. D. M., Hedges, C., et al., 2018
 Lightkurve: Kepler and TESS time series analysis in Python, Astrophysics Source Code Library, ascl:1812.013
 Lissauer, J. J., Ragozzine, D., Fabrycky, D. C., et al. 2011, *ApJS*, **197**, 8
 Lithwick, Y., & Wu, Y. 2012, *ApJL*, **756**, L11
 Maciejewski, G., Fernández, M., Aceituno, F. J., et al. 2015, *A&A*, **577**, A109
 Mann, A. W., Johnson, M. C., Vanderburg, A., et al. 2020, *AJ*, **160**, 179
 Masuda, K., & Winn, J. N. 2020, *AJ*, **159**, 81
 McArthur, B. E., Endl, M., Cochran, W. D., et al. 2004, *ApJL*, **614**, L81
 McKinney, W. 2010, in 9th Python in Science Conference, Vol. 445 (Austin, TX: SciPy), 51
 McLaughlin, D. B. 1924, *ApJ*, **60**, 22
 Michtchenko, T. A., Beaugé, C., & Ferraz-Mello, S. 2008a, *MNRAS*, **387**, 747
 Michtchenko, T. A., Beaugé, C., & Ferraz-Mello, S. 2008b, *MNRAS*, **391**, 215
 Millholland, S., Laughlin, G., Teske, J., et al. 2018, *AJ*, **155**, 106
 Muñoz, D. J., & Perets, H. B. 2018, *AJ*, **156**, 253
 NASA Exoplanet Archive 2023, Planetary Systems Composite Parameters, NExSci-Caltech/IPAC, doi:10.26133/NEA12
 Nealon, R., Pinte, C., Alexander, R., Mentiplay, D., & Dipierro, G. 2019, *MNRAS*, **484**, 4951
 Nelson, B. E., Ford, E. B., Wright, J. T., et al. 2014, *MNRAS*, **441**, 442
 Oliphant, T. E. 2006, *A Guide to NumPy*, Vol. 1 (USA: Trelgol Publishing)
 Pallé, E., Oshagh, M., Casasayas-Barris, N., et al. 2020, *A&A*, **643**, A25
 Petrovich, C., Malhotra, R., & Tremaine, S. 2013, *ApJ*, **770**, 24
 Rasio, F. A., & Ford, E. B. 1996, *Sci*, **274**, 954
 Rein, H. 2012, *MNRAS*, **427**, L21
 Rice, M., Wang, S., Gerbig, K., et al. 2023, *AJ*, **165**, 65
 Rice, M., Wang, S., Howard, A. W., et al. 2021, *AJ*, **162**, 182
 Rice, M., Wang, S., Wang, X.-Y., et al. 2022, *AJ*, **164**, 104
 Ricker, G. R., Winn, J. N., Vanderspek, R., et al. 2015, *JATIS*, **1**, 014003
 Ropert, S., Rojas, R., Suc, V., et al. 2021, *RMxAA*, **53**, 47
 Rossiter, R. A. 1924, *ApJ*, **60**, 15
 Salvatier, J., Wiecki, T. V., & Fonnesbeck, C. 2016, *PeerJ Comp. Sci.*, **2**, e55
 Sanchis-Ojeda, R., Fabrycky, D. C., Winn, J. N., et al. 2012, *Natur*, **487**, 449
 Sanchis-Ojeda, R., Winn, J. N., Dai, F., et al. 2015, *ApJL*, **812**, L11
 Schlafly, E. F., & Finkbeiner, D. P. 2011, *ApJ*, **737**, 103
 Snellgrove, M., Papaloizou, J., & Nelson, R. 2001, *A&A*, **374**, 1092
 Southworth, J. 2011, *MNRAS*, **417**, 2166
 STScI 2022, TESS Calibrated Full Frame Images: All Sectors, STScI/MAST
 Takaishi, D., Tsukamoto, Y., & Suto, Y. 2020, *MNRAS*, **492**, 5641
 Tayar, J., Claytor, Z. R., Huber, D., & van Saders, J. 2022, *ApJ*, **927**, 31
 Terquem, C., & Papaloizou, J. C. 2007, *ApJ*, **654**, 1110
 Trifonov, T., Brahm, R., Espinoza, N., et al. 2021, *AJ*, **162**, 283
 Turner, J. D., Ridden-Harper, A., & Jayawardhana, R. 2021, *AJ*, **161**, 72
 Virtanen, P., Gommers, R., Oliphant, T. E., et al. 2020, *NatMe*, **17**, 261
 von Essen, C., Schröter, S., Agol, E., & Schmitt, J. H. M. M. 2013, *A&A*, **555**, A92
 Voutsden, W. D., Farr, W. M., & Mandel, I. 2016, *MNRAS*, **455**, 1919
 Walt, S. V. D., Colbert, S. C., & Varoquaux, G. 2011, *CSE*, **13**, 22
 Wang, S., Addison, B., Fischer, D. A., et al. 2018, *AJ*, **155**, 70
 Wang, X.-Y., Rice, M., Wang, S., et al. 2022, *ApJL*, **926**, L8
 Wirth, C. P., Zhou, G., Quinn, S. N., et al. 2021, *ApJL*, **917**, L34
 Wong, I., Shporer, A., Vissapragada, S., et al. 2022, *AJ*, **163**, 175
 Wright, J., Rice, M., Wang, X.-Y., Hixenbaugh, K., & Wang, S. 2023, *AJ*, **166**, 217
 Yee, S. W., Winn, J. N., Knutson, H. A., et al. 2020, *ApJL*, **888**, L5
 Zhang, J., Weiss, L. M., Huber, D., et al. 2021, *AJ*, **162**, 89
 Zhao, L. L., Kunovac, V., Brewer, J. M., et al. 2023, *NatAs*, **7**, 198